ADVANCED MATERIALS
www.advmat.de

Prediction of Chronic Inflammation for Inhaled Particles: the Impact of Material Cycling and Quarantining in the Lung Epithelium

Hana Kokot, Boštjan Kokot, Aleksandar Sebastijanović, Carola Voss, Rok Podlipec, Patrycja Zawilska, Trine Berthing, Carolina Ballester-López, Pernille Høgh Danielsen, Claudia Contini, Mikhail Ivanov, Ana Krišelj, Petra Čotar, Qiaoxia Zhou, Jessica Ponti, Vadim Zhernovkov, Matthew Schneemilch, Zahra Doumandji, Mojca Pušnik, Polona Umek, Stane Pajk, Olivier Joubert, Otmar Schmid, Iztok Urbančič, Martin Irmler, Johannes Beckers, Vladimir Lobaskin, Sabina Halappanavar, Nick Quirke, Alexander P. Lyubartsev, Ulla Vogel, Tilen Koklič, Tobias Stoeger,* and Janez Štrancar**

On a daily basis, people are exposed to a multitude of health-hazardous airborne particulate matter with notable deposition in the fragile alveolar region of the lungs. Hence, there is a great need for identification and prediction of material-associated diseases, currently hindered due to the lack of in-depth understanding of causal relationships, in particular between acute exposures and chronic symptoms. By applying advanced microscopies and omics to in vitro and in vivo systems, together with in silico molecular modeling, it is determined herein that the long-lasting response to a single exposure can originate from the interplay between the newly discovered nanomaterial quarantining and nanomaterial cycling between different lung cell types. This new insight finally allows prediction of the spectrum of lung inflammation associated with materials of interest using only in vitro measurements and in silico modeling, potentially relating outcomes to material properties for a large number of materials, and thus boosting safe-by-design-based material development. Because of its profound implications for animal-free predictive toxicology, this work paves the way to a more efficient and hazard-free introduction of numerous new advanced materials into our lives.

While new exciting applications arise from rapid development of new advanced materials, their lifecycle, from production, processing, to degradation or even combustion, may inevitably result in the release of particulate matter into the environment.[1–3] According to the Organisation for Economic Co-operation and Development (OECD) and the World Health Organization (WHO), inhalation of particulate matter, predominantly of anthropogenic origin, is associated with several million human deaths globally every year.[4–6] While larger particles, deposited in airways, can be efficiently cleared from the bronchial region by the mucociliary escalator,[7] nanomaterials, the term used here for both submicron-sized particles (at least two dimensions below 1 µm) and nanoparticles (at least one dimension below 100 nm), can reach the alveolar region.[7,8] Due to the persistency

H. Kokot, B. Kokot, A. Sebastijanović, Dr. R. Podlipec, P. Zawilska, A. Krišelj, P. Čotar, M. Pušnik, Dr. P. Umek, Dr. S. Pajk, Dr. I. Urbančič, Dr. T. Koklič, Prof. J. Štrancar
Department of Condensed Matter Physics
Jožef Stefan Institute
Ljubljana 1000, Slovenia
E-mail: tilen.koklic@ijs.si; janez.strancar@ijs.si

The ORCID identification number(s) for the author(s) of this article can be found under https://doi.org/10.1002/adma.202003913.

DOI: 10.1002/adma.202003913

H. Kokot, A. Sebastijanović
Jožef Stefan International Postgraduate School
Ljubljana 1000, Slovenia

B. Kokot
Faculty of Natural Sciences and Mathematics
University of Maribor
Maribor 2000, Slovenia

Dr. C. Voss, Dr. C. Ballester-López, Q. Zhou, Dr. O. Schmid, Dr. T. Stoeger
Institute of Lung Biology and Disease
Helmholtz Zentrum München
85764 Neuherberg, Germany
E-mail: tobias.stoeger@helmholtz-muenchen.de

Dr. R. Podlipec
Ion Beam Center
Helmholtz-Zentrum Dresden-Rossendorf e.V.
01328 Dresden, Germany

of most nanomaterials, stemming from ineffective alveolar clearance,[9] even a single exposure can trigger chronic adverse conditions such as inflammation,[10–15] leading to lethal diseases, for example lung cancer, heart disease, and brain damage with accelerated cognitive decline.[16,17]

In order to facilitate the introduction of numerous new safe, hazard-free materials into our lives, the aforementioned adverse outcomes should be reliably predicted[18,19] using high-throughput alternatives to conventional testing strategies.[20] Despite advances in targeted test assays[21] and quantitative structure–activity relationship (QSAR)[22,23] models for nanotoxicology, currently neither in vitro nor in silico tools can reliably predict in vivo adverse outcomes,[24,25] and are, to our knowledge, especially unsuccessful in prediction of the systemic and chronic adverse effects.[26]

To improve the reliability of prediction, policy- and decision-makers around the world (OECD, United States Environmental Protection Agency, National Institutes of Health, European Comission, European Chemicals Agency, etc.) have highlighted the need to explain the molecular mechanisms involved and to define the key events in toxicity pathways governed by a chain of the material-specific bio–nano interactions. Only then do these adverse outcome pathways[27–29] gain their power in mechanism-based prediction of the apical endpoints using solely in vitro systems.

Here, we discovered new molecular key events and their causal relationships for respiratory toxicity of inhaled materials (**Figure 1**):

1. the process of nanomaterial quarantining (nanoquarantining) driven by enhanced lipid metabolism and resulting in immobile composites of nanomaterial and biological molecules on the cell surface that are termed cauliflowers, and
2. nanomaterial cycling between different lung cell types, fueled by a pro-inflammatory lipid-metabolism-associated influx of new leukocytes.

Based on this mechanistic understanding, we demonstrate the prediction of nanomaterial-induced chronic inflammation through three strategically selected in vitro tests and in silico modeling. As shown in **Table 1**, one of the key events, nanomaterial quarantining, has been observed in vitro in 9 out of 13 tested nanomaterials of different composition, shapes, and sizes, with the 9 all being metal oxides. The quarantining and all of the causal relationships within the nanomaterial cycling have been elaborated on the exemplary titanium dioxide nanotubes. The prediction, however, has been demonstrated using the here-discovered mechanism and validated for 5 tested (nano)materials (quartz, zinc oxide, titanium dioxide nanotubes and nanocubes) qualitatively against in vivo experimental data from day 28 after nanomaterial instillation using the lowest dose with an observed inflammatory/adverse effect (lowest observed adverse effect level, LOAEL, at >5% of bronchoalveolar liquid polymorphonuclear cells—BAL PMN).

Quarantining of Nanomaterials: To uncover the causal relationships between events leading from pulmonary nanomaterial exposure to chronic inflammation, we applied a comprehensive set of complementary in vivo, in vitro, and in silico experiments employing state-of-the-art microscopy, spectroscopy, omics, and modeling approaches. TiO_2 nanotubes were selected as the exemplary material for the following reasons. First, they induce high and long-lasting subacute or even chronic inflammatory responses in vivo (Section S2d, Supporting Information). Second, the cells remain viable in vitro for longer period after exposure. Third and crucially, this nanomaterial can be reliably fluorescently labeled, enabling detailed study of the mechanism of the inflammatory response and exploration of the causal relationships among key molecular events in living cells. And last but not least, this nanomaterial induces the formation of cauliflowers

Dr. T. Berthing, Dr. P. H. Danielsen, Prof. U. Vogel
National Research Centre for the Working Environment
Copenhagen Ø 2100, Denmark
Dr. C. Contini, Dr. M. Schneemilch, Prof. N. Quirke
Department of Chemistry
Molecular Sciences Research Hub
Imperial College London
London W12 0BZ, UK
M. Ivanov, Prof. A. P. Lyubartsev
Department of Materials and Environmental Chemistry
Stockholm University
Stockholm SE-10691, Sweden
P. Čotar
Faculty of Mathematics and Physics
University of Ljubljana
Ljubljana 1000, Slovenia
Q. Zhou
Department of Forensic Pathology
Sichuan University
Chengdu 610065, China
Dr. J. Ponti
European Commission
Joint Research Centre (JRC)
Ispra 21027, Italy
Dr. V. Zhernovkov
Systems Biology Ireland
School of Medicine
University College Dublin
Belfield, Dublin 4, Ireland
Dr. Z. Doumandji, Dr. O. Joubert
Institut Jean Lamour, UMR CNRS 7198
Université de Lorraine
CNRS, IJL, Nancy F-54000, France
M. Pušnik, Dr. S. Pajk
Faculty of Pharmacy
University of Ljubljana
Ljubljana 1000, Slovenia
Dr. M. Irmler, Prof. J. Beckers
Institute of Experimental Genetics
Helmholtz Zentrum München
85764 Neuherberg, Germany
Prof. J. Beckers
German Center for Diabetes Research (DZD)
85764 Neuherberg, Germany
Prof. J. Beckers
Chair of Experimental Genetics, Center of Life and Food Sciences, Weihenstephan
Technische Universität München
85354 Freising, Germany
Prof. V. Lobaskin
School of Physics
University College Dublin
Belfield, Dublin 4, Ireland
Prof. S. Halappanavar
Environmental Health Science and Research Bureau
Health Canada
Ottawa K1Y 0M1, Canada

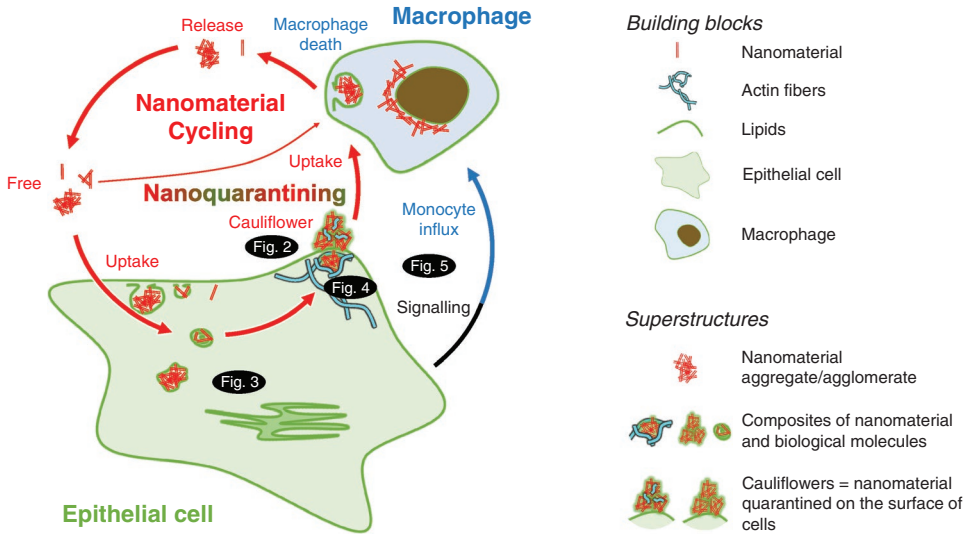

Figure 1. Scheme of the discovered cycle of nanomaterial on the lung alveolar surface model with associated key molecular events that drive chronic inflammation following the exposure to nanomaterials together with a legend of graphical elements (pictograms), used in this and the following figures. The reader is encouraged to refer to this scheme and legend during elaboration of individual events later in the text (noted in black ellipses with referring figure numbers).

(i.e., nanomaterial is quarantined) on the surface of epithelial lung cells both in vitro (**Figure 2**C) and in vivo (Figure 2B, violet structures). Because similar structures are observed after exposure to crystalline quartz (DQ12; Figure 2C; Section S2c, Supporting Information), a well-known occupational hazard causing chronic pulmonary inflammation,[10] we hypothesized that the cell-surface localized cauliflowers might be causally related to chronic inflammation. In order to test the hypothesis, nanomaterial delivery has been optimized to mimic exposure conditions and reproduce the nanoquarantining observed in vivo.[39]

Based on previously observed strong interactions between TiO_2 nanotubes and epithelial plasma membranes[40] we would expect that at higher surface doses (ratio of surface of nanomaterial versus cell surface 10:1 or more) these nanoparticles could completely disrupt epithelial cell membranes (relevance of dose explained in Section S0i, Supporting Information). Surprisingly, our experiments show that the tested epithelial cells survive exposure to surface doses as high as 100:1 (Figure 2E; Sections S0e and S0f, Supporting Information) resembling doses that may appear unrealistic but actually frequently occur in "hot spots" as described for in vivo experiments.[41] Notably, a few days after the exposure, the majority of the nanoparticles are found in large composites of nanomaterial and biological molecules on the epithelial surface, consisting of at least nanoparticles and lipids, which we termed cauliflowers because of their shapes in our fluorescence micrographs (Figure 2D,E, yellow color, Figure 2F).

Because the cauliflowers need several days to form and contain excessive amounts of lipids, we next explore changes to the membrane structures and the lipid metabolism in an active biological response to the nanomaterial exposure.

The Role of Lipids: Coinciding with the formation of the lipid-rich cauliflowers (**Figure 3**B), that is, 2 days after the nanomaterial exposure, a strong upregulation of lipid-metabolism-related genes is observed (Figure 3D). Moreover, further modulation of the lipid synthesis pathway by blocking one of its key enzymes, fatty acid synthase (FAS), with resveratrol precludes the formation of large cauliflowers (Figure 3I), confirming that the epithelial cells actively respond to the nanomaterial exposure with increased lipid synthesis. Apparently, the additionally synthesized lipids are used to immobilize and quarantine the hazardous nanoparticle surface, rendering such composites more loosely packed compared to the aggregates/agglomerates of pure nanoparticles, as demonstrated by an increased fluorescence lifetime (FLIM, Figure 3C). This process enables the layered growth of the cauliflowers over time, hindering any further interaction and lowering the active dose of the nanomaterial.

As the internalization of the nanoparticles typically precedes the cauliflower formation (Section S3b, Supporting Information), we investigate the causal relationship between the two phenomena by blocking an important route of nanoparticle uptake, that is, clathrin-mediated endocytosis (Section S0d, Supporting Information), using chlorpromazine. Interestingly, small "proto" cauliflowers are formed soon after exposure (15 min time scale; Figure 3G), indicating an additional mechanism of formation that requires no intracellular processing. In this case the formation of cauliflowers presumably relies on the strong physical affinity between the nanoparticles and the lipids, which is supported by the in silico simulations (Figure 3E) and the in vitro experiments on model lipid membranes (Section S0c, Supporting Information). However, these "proto" cauliflowers are rarely seen under normal conditions, which leads us to conclude that this additional mechanism of formation is usually less likely, possibly due to the efficient particle uptake that displaces the nanomaterials away from the plasma membrane, preventing their further interaction.

Interestingly, the depletion of cholesterol as the major membrane constituent by beta-methyl-cyclodextrin, which increases the fluidity of the plasma membrane, leads to a strong suppression of rapid (membrane-lipid-drain only) cauliflower formation (Figure 3H). This indicates an important interaction between the nanoparticles and the cholesterol, which is also reflected in the strongly upregulated cholesterol and lipid

Table 1. Short overview of nanomaterials used in this study. The extended version along with TEM images and corresponding in vivo inflammation data for the nanomaterials can be found in Section S0b, Supporting Information. Empty spaces represent not-yet-determined values. The prediction is validated qualitatively against in vivo experimental data obtained at day 28 after nanomaterial instillation in mice or rats, the so-called subacute lung inflammation, a prestage required for the development of chronic lung inflammation. The criterion for a material causing long-lasting inflammation in vivo is that the lowest dose with an observed effect (LOAEL at >5% of BAL PMN cells) is smaller than 1:10 (surface area of nanomaterial:surface area of lungs).

Nanomaterial name (chemistry and morphology)	ID (JRC code)	Dimensions (width × length in [nm])	BET surface [$m^2\ g^{-1}$]	Nanomaterial quarantining observed	Prediction applicable	Prediction demonstrated and validated	LOAEL (lowest surface dose with observed effect)
TiO_2 (anatase) nanotubes	TiO_2 tubes (n.a.)	10 × 100[10]	152[10]	✓	✓	✓	1:20[10]
TiO_2 (anatase) nanocubes	TiO_2 cubes (n.a.)	15 × 20[10]	97[10]	✓	✓	✓	not observed up to 1:3[10]
TiO_2 (anatase) nanospheres small	MKN-TiO_2-A015 (n.a.)	16–28[10]	74[10]	✓	✓		Not observed up to 1:4[10]
TiO_2 (anatase) nanospheres large	MKN-TiO_2-A100 (n.a.)	12–50[10]	85[10]	✓	✓		Not observed up to 1:4[10]
TiO_2 rutile–anatase	NM-105 (JRCNM01005a)	20[30]	46[30]	✓	✓		Not observed up to 1:7[31]
TiO_2 anatase	NM-101 (JRCNM01001a)	5[30]	230[30]	✓	✓		Not observed up to 1:1.3[31]
SiO_2 crystalline	DQ12 quartz (n.a.)	960[10]	10[10]	✓	✓	✓	1:33[10]
SiO_2 amorphous	NM-200 (JRCNM02000a)	20[32]	189[32]	✗	✓		n.d.
ZnO uncoated	NM-110 (JRCNM62101a)	158[33]	12[33]	✓	✓	✓	n.d.[34]
ZnO coated	NM-111 (JRCNM01101a)	152[33]	15[33]	✓	✓	✓	n.d.[34]
Multiwall carbon nanotubes—thin	NM-402 (JRCNM04002a)	11 × 1400[35]	226[35]	✗			1:13[36]
Multiwall carbon nanotubes—thick	NM-401 (JRCNM04001a)	67 × 4000[35]	18[35]	✗	✗		1:100[37]
Carbon black	Printex 90 (n.a)	14[38]	300[38]	✗			1:1[38]

synthesis pathways in the epithelial cells in vitro (Figure 3D, heatmap; Section S3d, Supporting Information), as well as in mouse lungs in vivo (Section S3d, Supporting Information). In the case of cholesterol-depleted plasma membranes, the majority of the nanoparticles cross the plasma membranes on a timescale of minutes, resulting in a fine distribution of the particles inside the cell. The dominant role of such a passage can also be observed when the nanoparticles are delivered in a highly dispersed form through an aerosol directly to the epithelial plasma cell membranes and pass through them[42] in a matter of seconds (Figure 3F and Video S1, Supporting Information).

For the alveolar barrier of the lung in particular, the lipid-synthesis-driven formation of cauliflowers appears to be an important part of the protective response of alveolar epithelial cells, enabling their survival after exposure to the nanomaterial, even at higher doses (Sections S0e and S0g, Supporting Information). As we consistently observed the quarantining of the nanomaterials on the cell surface that follows the nanomaterial internalization, we further explore the cellular mechanisms that facilitate the export of the internalized material.

The Role of Actin: As exocytosis involves cytoskeletal actin remodeling, we examined the role of actin in the process of cauliflower formation. Almost simultaneously with nanoparticle uptake and well before cauliflower formation, many nanoparticles interact with actin fibers (**Figure 4**D), forming nanoparticle–actin 3D composites resembling Faberge eggs (Figure 4B). Hours after exposure, the same interaction causes actin network transformation from linearly aligned to branched fibers (Figure 4E), which is associated with an increased cell motility[43] as well as with internal vesicular trafficking[44,45] and exocytosis.[46,47]

By blocking the actin fiber dynamics (polymerization and depolymerization) with jasplakinolide, the excretion of exocytotic vesicles can be stopped, thereby enabling the simultaneous visualization and identification of the nanoparticles trapped in the exocytotic vesicles (actin rings; Figure 4C). As actin can be identified extracellularly within the cauliflowers (Figure 4F and Video S2, Supporting Information), the excretion of nanoparticles is apparently more destructive to the actin network than normal homeostatic exocytosis, where actin is retained inside the cells. Actin adherence to the nanomaterial is also reflected in the coronome analysis of the mobile fraction of nanoparticles after the exposure, in which we have previously detected an abundant fraction of actin proteins, but were unable to explain it.[40] The loss and destruction of actin also triggers the upregulation of the pathways related to actin synthesis (Figure 4G).

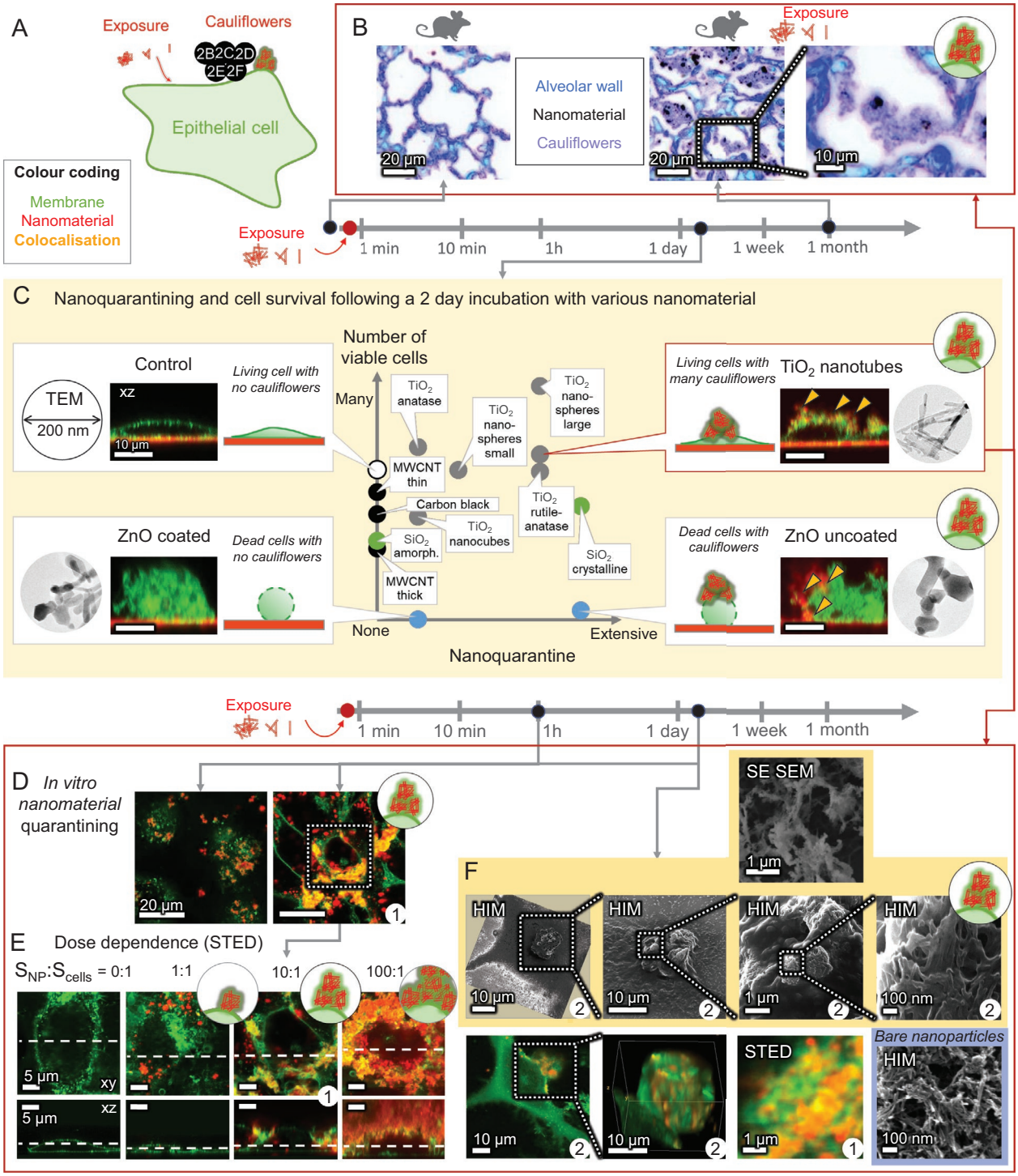

Figure 2. Nanomaterial quarantining (nanoquarantining)—formation of bio–nano composites on epithelial cell surface, referred to as "cauliflowers." A) A general scheme of events shown in this figure. B) Hyperspectral color-inverted dark-field microscopy images of TiO_2 nanotubes (black) in cauliflowers (violet) observed in alveoli (blue) one month after instillation of the nanomaterial in mice. C–F) In the fluorescence microscpy images of in vitro alveolar epithelial (LA-4) cells, membranes are shown in green and nanoparticles in red. Images with the same number in the lower-right corner are images of the same cell. C) Presence of cauliflowers, cell survival and *xz* cross sections after a 2-day exposure to several nanomaterials at a nanomaterial-to-cell surface ratio (S_{NP}:S_{cells}) of 10:1 (nanoparticles observed in backscatter). The insets show 200-nm-large transmission electron microscopy (TEM) images of the nanoparticles used. D) Time-dependent cauliflower formation by LA-4 exposed to TiO_2 nanotubes at S_{NP}:S_{cells} = 10:1. E) Super-resolved stimulation emission depletion (STED) *xy* and *xz* cross sections of dose-dependent cauliflower growth reveal that cauliflowers are located on the outer surface of cells after 2 days. S_{NP}:S_{cells} are 0:1, 1:1, 10:1, and 100:1. F) High-resolution correlative STED, secondary-electron scanning electron microscopy (SE SEM), and helium-ion microscopy (HIM) images reveal the detailed structures of cauliflowers at a S_{NP}:S_{cells} = 10:1 (see also Video S3, Supporting Information). For associated data, see Section S2, Supporting Information.

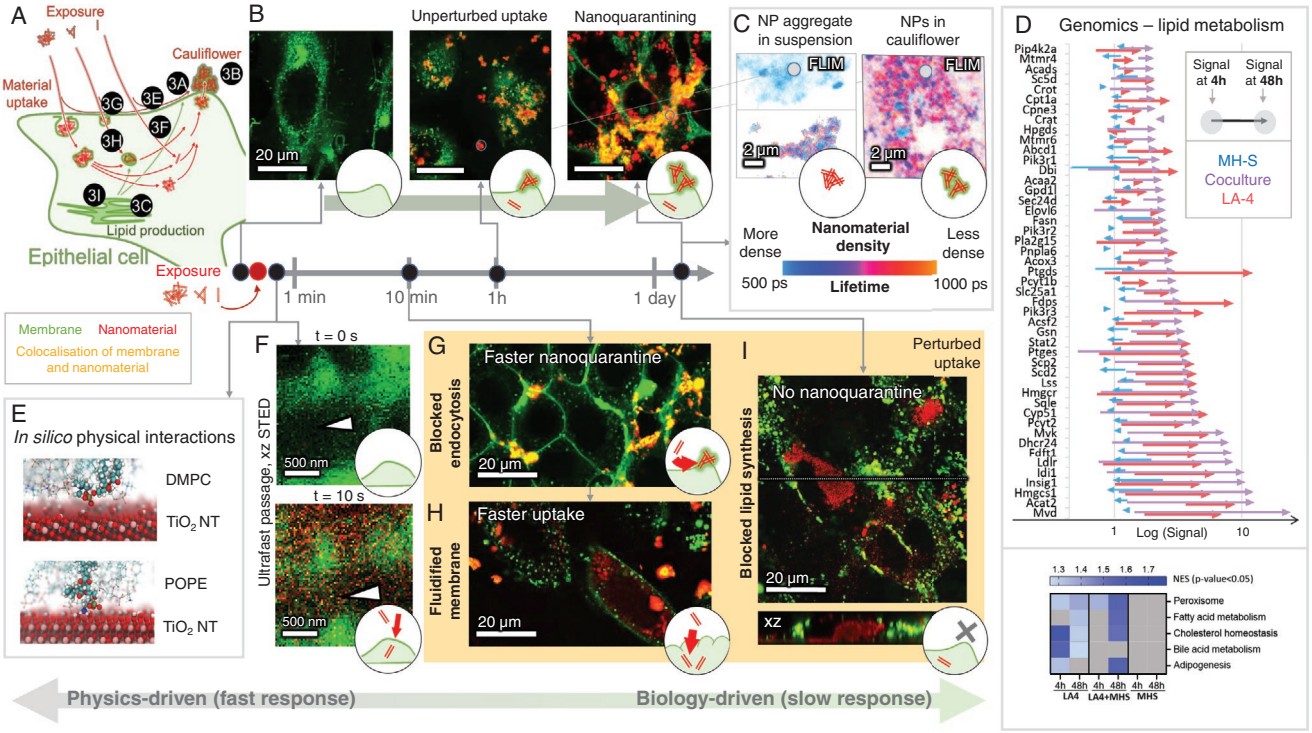

Figure 3. Role of lipids in nanomaterial quarantining (nanoquarantining)—cauliflower formation. A) General scheme of events. In fluorescence micrographs in vitro, cell membranes are displayed in green and TiO_2 nanotubes in red, surface dose was 10:1 (except (F)). B) Unperturbed uptake of TiO_2 nanotubes after 0, 1 h, and 2 days by epithelial LA-4 lung cells, same as Figure 2D. C) Increased fluorescence lifetime (FLIM) of fluorophore on TiO_2 nanotubes in cauliflowers (right) compared to passively formed nanomaterial aggregates/agglomerates in suspension (left) corresponds to increased distance between fluorophores on the nanotubes (e.g., separation due to lipid interspacing). D) Transcriptional signature of lipid metabolism genes (top) and hallmark gene sets (bottom) for MH-S macrophages (blue), LA-4 epithelial cells (red), and their co-culture (purple) after 4 h (beginning of arrow) and 48 h (end of arrow) of nanomaterial exposure; normalized enrichment scores with p-value < 0.05 are shown. E) Final state of full-atom in silico simulation confirms strong interaction between disordered lipids and the TiO_2 nanotubes (movies and 3D of DMPC: Video S4, Video S5, Supporting Information, and of POPE: Video S6, Video S7, Supporting Information). F) *xz* cross sections immediately before (above) and 10 s after (below) instant delivery of TiO_2 nanotubes onto cells by nebulization (1:1 surface dose) show ultrafast membrane passage of the nanotubes through the cell plasma membrane into the cell (arrowhead) (see Video S1, Supporting Information). Drug-perturbed uptakes (to compare with (B)). G) Chlorpromazine-blocked clathrin-mediated endocytosis (see Video S8, Video S9, Supporting Information); H) fluidified cell plasma membrane induced by cholesterol depletion (beta-methyl-cyclodextrin) (see Video S10, Supporting Information). I) inhibited fatty-acid synthesis (resveratrol-blocked fatty-acid synthase) (see Video S11, Supporting Information). For associated data, see Section S3, Supporting Information.

The formation of cauliflowers on the cell surface thus involves both membrane lipids and actin (heatmaps in Figure 4C,D) that directly interact with the nanoparticle surface. Due to the strong binding of the amines and phosphates identified by in silico simulations (Figure 3E), it is reasonable to expect that various biomolecules, including lipids, proteins, and nucleic acids, strongly bind to the same particle surface. Moreover, multiple binding sites on the nanomaterial and biomolecules or their supramolecular structures lead directly to crosslinking and the formation of the observed large cauliflowers. This implies that a lack of strong interaction identified within the in silico modeling of biomolecule-nanomaterial surface pairs, is predictive of the absence of cauliflower formation, and can be used for safety prediction of new nano- or related advanced materials.

The ability of the alveolar epithelium to supply enough biomolecules to crosslink and thereby quarantine the received dose of nanomaterial explains the cell survival, even for relatively large local doses of nanomaterials, which can also be observed in vivo (Figure 2). The process of nanomaterial quarantining, however, seems to contradict the observation of simultaneous chronic pulmonary inflammation, raising the question of the role of neighboring cell types, especially alveolar macrophages, which are responsible for the alveolar immune defense and thereby the alveolar integrity. To address this, we expose a co-culture of LA-4 epithelial cells and MH-S alveolar macrophages in the same way as we did with the epithelial monoculture.

Macrophage Action against Epithelial Defense: With a co-culture of MH-S alveolar macrophages on top of nearly confluent LA-4 epithelial cells we aimed to mimic the cell populations of the alveolar surface, where alveolar macrophages represent approximately 3–5% of all the alveolar cells.[48] Upon exposure of the co-culture to TiO_2 nanotubes, part of the material becomes internalized by the phagocytes, which are however too slow to clear the nanomaterial and are therefore unable to prevent it from reaching the epithelial cell surface (Section S0h, Supporting Information). This is in line with previous in vivo observations.[49] Aside from that, motility of macrophages decreases considerably after having taken up large amounts of nanoparticles (graph in Section S0h, Supporting Information), making their clearance function even less efficient. The incomplete clearance explains why the exposed epithelium also produces cauliflowers in co-culture (Section S0h, Supporting Information), reproducing the cauliflowers observed in vivo in the alveolar region of the lungs of particle-exposed mice (Figure 2B).

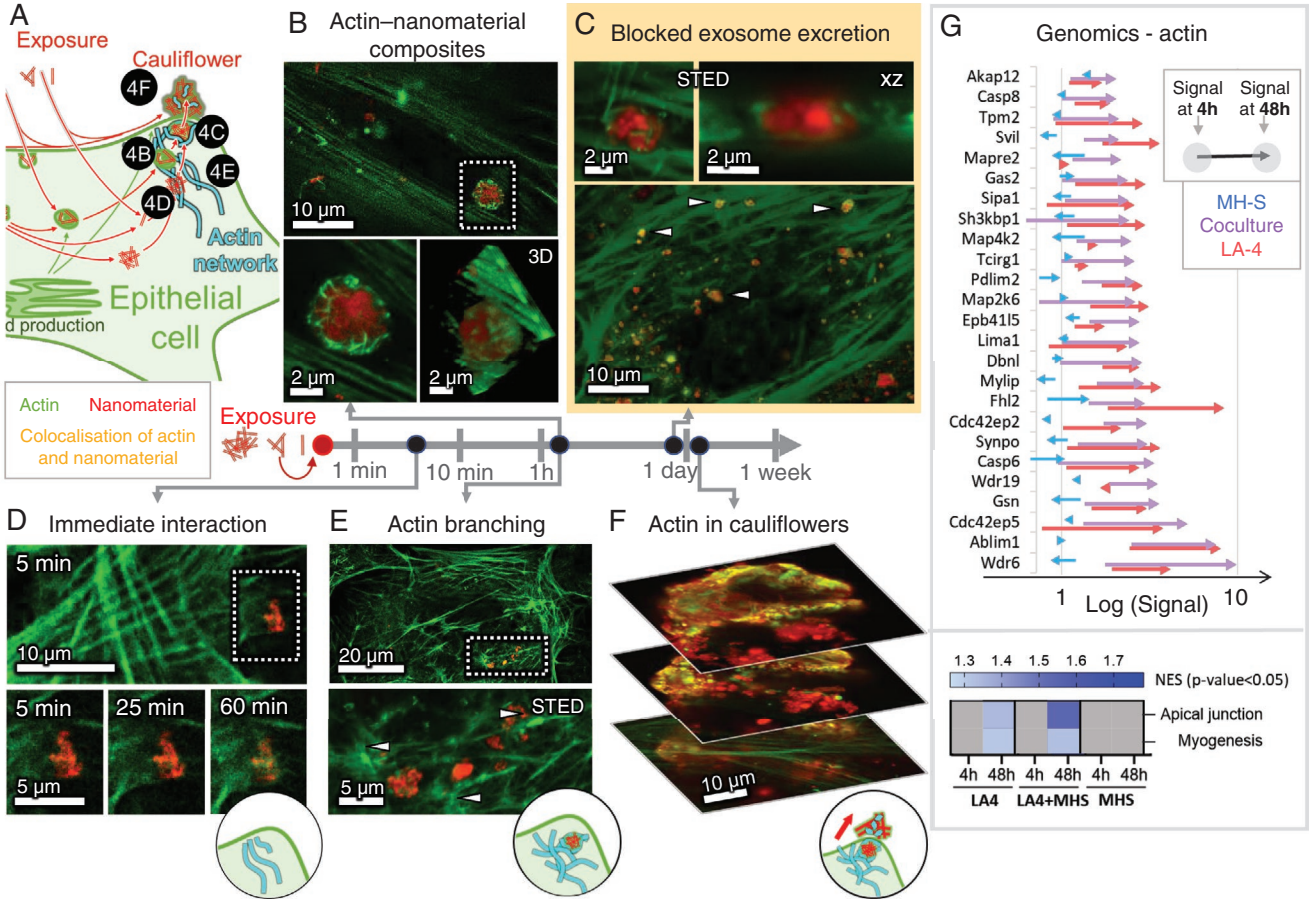

Figure 4. Role of actin in nanomaterial quarantining (nanoquarantining)—cauliflower formation. A) General scheme of events. Fluorescence microscopy images of the actin network of LA-4 cells (green) after exposure to TiO_2 nanotubes (red) at a 10:1 surface dose. D) Soon after exposure, actin interacts with internalized nanoparticles (see also Video S12, Supporting Information). B) This leads to formation of actin–nanoparticle composites after a few hours (see also Video S13, Supporting Information). E) Synchronously, the actin network branches (arrowheads), indicating changes in internal processes and reshaping of the cell. C) Blocking the final stage of exocytosis with jasplakinolide traps nanoparticles in actin rings, prepared for exocytosis (arrowheads and zoom-ins) (see also Video S14, Supporting Information). F) After a few days, actin fragments are observed in cauliflowers (see also Video S2, Supporting Information). G) Transcriptional signature of actin-network-related genes (top) and hallmark gene sets (bottom) for LA-4 (red), macrophages (blue), and their co-cultures (purple) after 4 h (beginning of arrow) and 48 h (end of arrow) of nanomaterial exposure. For associated data, see Section S4, Supporting Information.

Although the nanoparticles get quarantined in cauliflowers on the surface of the LA-4 cells, enabling their survival, the same structures seem to trigger the attack of macrophages, as seen in the experiment when unexposed macrophages were added to pre-exposed and therefore cauliflower-rich epithelium (**Figure 5**A). After internalization of the cauliflowers, macrophages are able to degrade only their organic part, as revealed by the decreased lifetime of the fluorescent probes bound to the nanoparticles, indicating denser packing of the nanoparticles in macrophages compared to the cauliflowers (FLIM maps in Figure 5A insets). This releases nanoparticles from the composite and exposes the macrophage interior to the bare nanoparticles' surface, leading to macrophage death and subsequent disintegration, as observed in monocultures (Figure 5D and Video S15, Supporting Information). This macrophage susceptibility might be related to the lack of exocytosis and unchanged lipid synthesis signature (Figure 3C). A similar macrophage fate is also observed after attacking epithelial cells (Figure 5E and Video S16, Supporting Information) or other macrophages with internalized nanomaterials (Figure 5F and Video S17, Supporting Information). When nanomaterial-exposed macrophages die, they release bare nanomaterial, which is subsequently taken up again by the epithelial cells. This can be observed experimentally: after nanomaterial-laden macrophages were added to unexposed untreated epithelial layer, nanoparticles can again be localized inside epithelial cells (Figure 5B).

This uptake, in turn, leads to quarantined nanomaterial on the self-protected epithelial cells. In vivo, however, dead macrophages can be replaced through an influx of new monocyte-derived macrophages, attracted by respective macrophage/monocyte chemo-attractants such as the C-C motif ligand 3 [Ccl3]), released from adjacent epithelial cells, or Ccl2 and Ccl17 for the lungs of nanomaterial-exposed mice (Section S3d, Supporting Information). This macrophage replenishment brings the entire system to conditions very similar to the initial exposure, while the reuptake of the nanomaterial by the epithelium finally closes the chain of events, together forming a vicious cycle, generating a never-before-seen loop of persistent inflammation (Figure 1 and Figure 5G).

Strikingly, the same chemokine expressions can be detected both in vivo (Figure 5C inset) and in vitro in the co-culture of

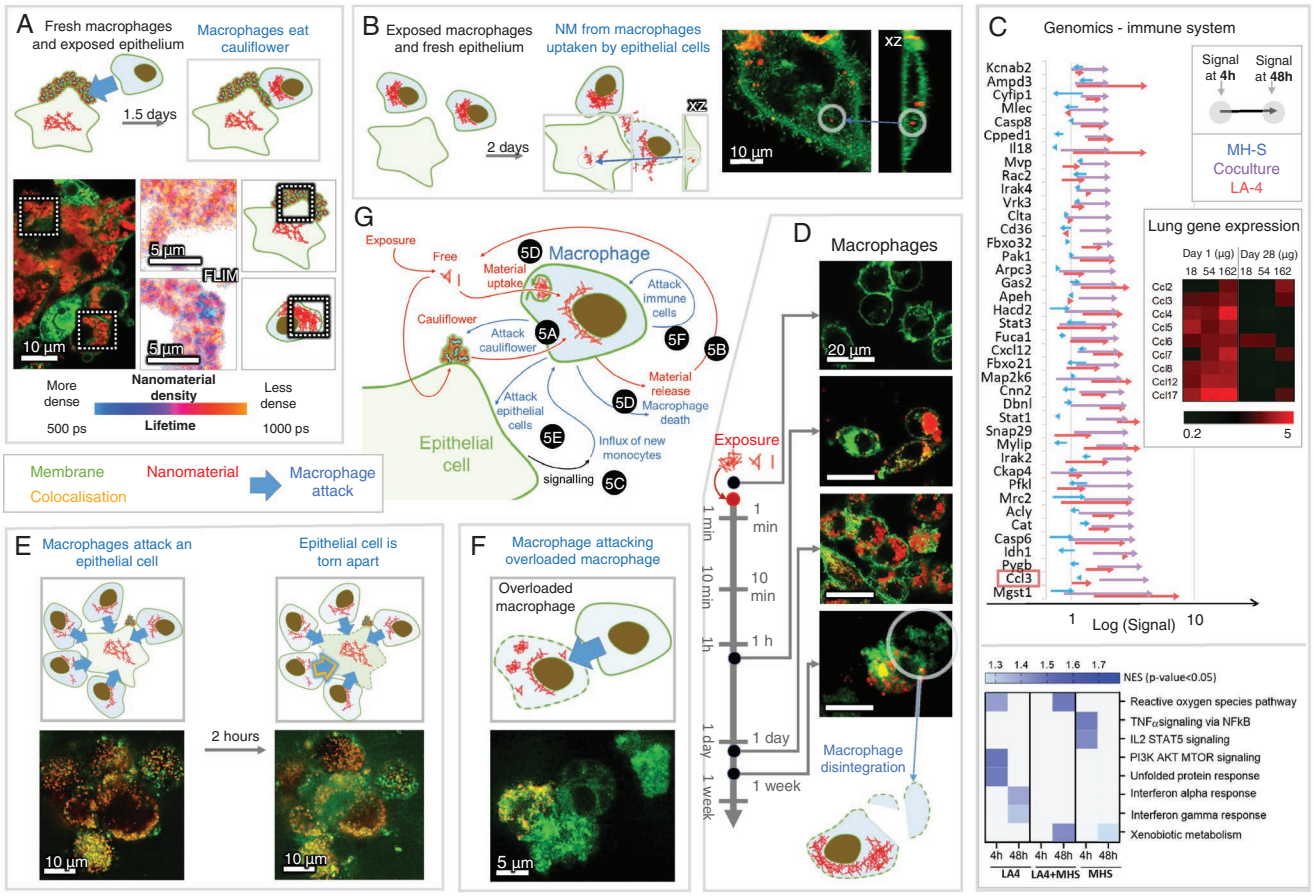

Figure 5. The cycle of uptake, quarantine, and release in nanomaterial-exposed co-culture. In all fluorescence micrographs, cell membranes are displayed in green and TiO_2 nanotubes in red, and the surface dose of nanoparticles is 10:1. A) Unexposed macrophages (MH-S) were added to washed LA-4 cells with cauliflowers. Within 1.5 days, MH-S phagocyte the cauliflowers from the LA-4 cell surface, and degrade their organic (lipid) part, thereby compacting the nanoparticles (fluorescence-lifetime-maps FLIM, right). B) Washed nanomaterial-laden MH-S were added to unexposed LA-4. After 2 days, the nanomaterial is found in LA-4 cells (encircled). C) Transcriptional signature of genes related to the immune response (top) and hallmark gene sets (bottom) for LA-4 (red), MH-S (blue), and their co-culture (purple) after 4 h (beginning of arrow) and 48 h (end of arrow) of nanomaterial exposure, with lung gene expression of some CCL monocyte attractants after 1 and 28 days shown in the inset. D) Nanoparticle uptake by MH-S followed by their disintegration after a few days (encircled): see Video S18 and Video S19 (control), Video S20 and Video S21 (2 h), Video S22 and Video S23 (2 days), Video S15 (4 days, MH-S disintegration) in the Supporting Information. E) Time lapse of MH-S attacking and tearing apart a nanomaterial-laden LA-4 cell (see also Video S16, Supporting Information). F) Observation of MH-S attacking another nanomaterial-laden macrophage (see also Video S17, Supporting Information). G) A general scheme of events shown in this figure. For associated data, see Section S5, Supporting Information.

LA-4 and MH-S cells (Figure 5C, purple arrows), but not in the monocultures of LA-4 (Figure 5C, red arrows) nor of MH-S (Figure 5C, blue arrows). This pro-inflammatory signaling represents the last missing piece of evidence that this particular in vitro co-culture can reproduce the entire cycle of the chronic-inflammation-initiating mechanism (black arrow in Figure 5G). Can we thus predict such an in vivo chronic inflammation response by measuring the specific states of simple in vitro tests?

Acute or Chronic? The Birth of Predictive Tools: The proposed pathway (Figure 1), connecting an acute nanoparticle exposure to a chronic inflammation via a chain of causally related events, allows us to construct a simplified cyclical theoretical model that describes the flow of the nanomaterial between four separate compartments: i) outside the cells, ii) inside the epithelial cells, iii) quarantined in cauliflowers, and iv) inside macrophages. This model is defined with three key descriptors (Section S6a, Supporting Information, depicted in **Figure 6**A), measurable in appropriate in vitro assays for any nanomaterial of interest (yellow shaded boxes in Figure 6A):

1. The rate of toxicity of the nanomaterials to individual cells (*tox*) is determined by the measured number of viable macrophages in a MH-S monoculture after 4 days of exposure (Figure 6A, toxicity);
2. The rate of nanomaterial quarantining by epithelial cells (*cff*) is calculated from the measured fraction of nanomaterial in the cauliflowers in the LA-4 monoculture after 2 days of exposure (Figure 6A, quarantining) taking into account the correction due to the rate of toxicity of the nanomaterials to individual cells (*tox*);
3. The efficiency of the signaling and the monocyte influx replacing the dying macrophages (*signalEff*) is calculated either from the measured release of macrophage attractants in the in vitro co-culture of LA-4 and MH-S after 2 days of exposure or from the measured influx of inflammatory cells (leukocyte) in vivo after at least 10 days (Figure 6A, signaling), a time point where the chronification of the response is started; the calculation includes the corrections due to the rate of toxicity of the nanomaterials to individual cells (*tox*) as well as due to the rate of nanomaterial quarantining by epithelial cells (*cff*).

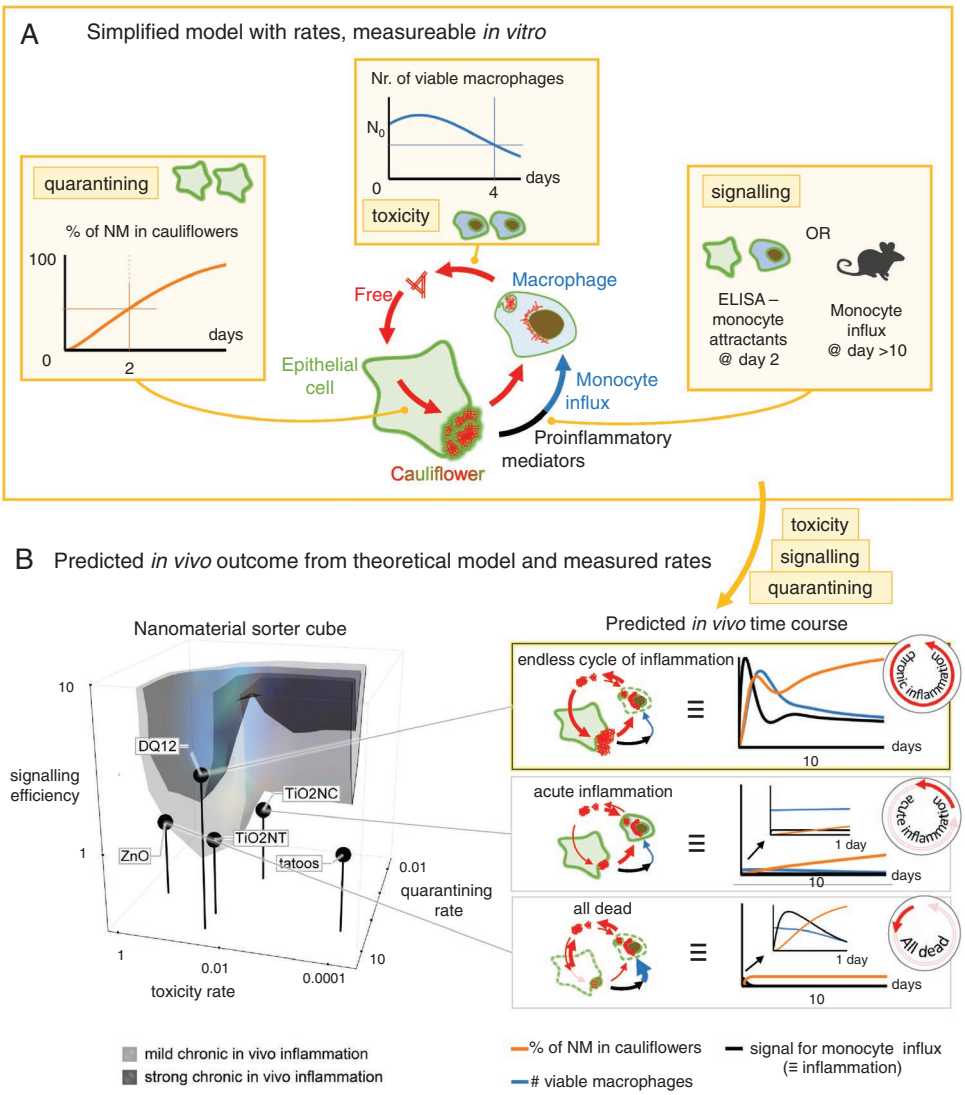

Figure 6. A) Theoretical model, defined by the rates of nanomaterial quarantining—cauliflower formation, nanomaterial toxicity, and signaling efficiency. These nanomaterial descriptors can be determined from single time-point measurements in vitro and/or in vivo. B) The model is evaluated using these determined parameters, producing in vivo time courses (right) of the relative amount of nanomaterial in cauliflowers (orange), the number of viable macrophages (blue) and the signal for their influx (black). The value of the latter at day 10, when the acute inflammation is expected to subside, converging to in vivo measurements at day 28, is contoured in the 3D space of the aforementioned rates (cube on the left). Nanomaterials are placed in the same 3D cube according to their measured descriptors, enabling the prediction of the degree of nanoparticle-induced chronic inflammation. For associated data, see Section S6, Supporting Information.

Whether the cycle stops or continues indefinitely depends heavily on the rates of the associated processes, calculated from the measured descriptors as described in Section S6a, Supporting Information. Using these rates, the model can predict the in vivo time course of the amount of quarantined nanomaterial in the cauliflowers, signaling for immune cells influx, as well as of the total macrophage number, and accordingly predict the nanomaterial-specific acute-to-chronic inflammation outcome (Figure 6B, time traces). For example, for very toxic nanomaterials, such as ZnO, the model yields a rapid decline in the number of cells, resulting in the destruction of the alveolar layer, which is consistent with the in vivo observations.[51] For a material with an intermediate toxicity and quarantining rate, for example TiO_2 nanocubes, the model predicts weak transient inflammation, with all the nanomaterial ending up in cells, as observed in vivo.[10] Finally, for a material such as TiO_2 nanotubes or DQ12 with intermediate toxicity and a high quarantining rate, persistently high inflammation and large cauliflowers (Figure 6B, time traces) are predicted, reproducing the in vivo observations (Figure 2B). In this 3D space of nanomaterial descriptors (Figure 6B–D, plot) we can now delineate regions eliciting a similar outcome, thus sorting nanomaterials according to their mode of action.

Conclusions and Perspectives: Among various materials that we are daily exposed to, natural; engineered; and processing-, combustion-, and degradation-originating nanomaterials constitute a large and potentially health-hazardous class of materials with

notable deposition in the lung alveolar region due to their submicron size. While their toxicity assessments represent one of the main societal priorities, the lack of clear causal relationships between acute exposures and prolonged or even chronic symptoms still prevents a reliable, let alone high-throughput prediction of nanomaterial-induced diseases, necessitating case-by-case in vivo animal testing.

While tracking the molecular events upon nanomaterial exposure in vitro, using the minimal monoculture or co-culture system without surfactant capable of reproducing the events observed in vivo, we have first discovered an unexpected lung epithelial cell defense mechanism. Namely, the lipid-mediated nanomaterial quarantining prevents acute epithelium damage and delays the inevitable macrophage death. The nanomaterial, released from the macrophages, is then taken up again by epithelial cells imposing an additional delay with regard to the original exposure, which in turn starts to feed the continuous cycling of nanomaterial between epithelial and immune cells. The delay (expansion over a large time window) is crucial for transformation of an acute inflammation into a chronic one through continuous stimulation of (the cycle of) the molecular events leading to prolonged and continuous release of pro-inflammatory mediators and subsequent chronic inflammation.

Second, the unraveled pathway allowed us to predict the in vivo outcome, being either acute inflammation or a long-term chronic one, using in silico modeling fed by only a few strategically selected in vitro measurements:

1. measuring cell viability of the nanomaterial-exposed macrophages (monoculture);
2. measuring the fraction of nanomaterial quarantined on the surface of epithelial cells (monoculture);
3. determining the release of macrophage/monocyte attractants in co-culture of epithelial cells and macrophages, or alternatively, determining the recruitment of inflammatory cells in vivo.

Generally, the prediction is applicable to any nanomaterial, regardless of its specific properties, such as shape, size, charge, surface functionalization, solubility, and intrinsic toxicity. However, in this form it can produce false-negative result if no nanoquarantining can be observed, indicating that chronic inflammation is in this case triggered by another, yet undiscovered mechanism (e.g., multiwall carbon nanotubes, the JRC NM401, with particular high cytotoxicity to phagocytes[52,53]).

Based on this, we contend that the game-changing screening strategy in material safety assessment should be based on understanding the response of the organism to nanomaterial exposure from the initial contact with the nanomaterial to the potential adverse outcome. Such a mechanistic understanding ultimately requires multidisciplinary approaches, as shown here by combining advanced imaging, omics, particle labeling, and tracking techniques applied in vivo and in vitro with in silico modeling that jointly yield novel, high-throughput, alternative-to-animal testing strategies. This can also enrich our knowledge on relations between material properties and adverse outcomes for a variety of materials, boosting safe-by-design-based material development.

Experimental Section

This is a condensed description of the methods. Details are available in Section S0a, Supporting Information; for general methods as well as for each experiment separately, see S1–S6.

Materials: Alexa Fluor 647 NHS ester (Thermo Fisher), Star 520 SXP NHS ester (Abberior), ATTO 594 NHS ester (Atto-tec), CellMask Orange (Invitrogen), SiR Actin (Cytoskeleton), Star Red-DPPE (Abberior), 4-(8,9-dimethyl-6,8-dinonyl-2-oxo-8,9-dihydro-2H-pyrano[3,2-g]quinolin-3-yl)-1-(3-(trimethylammonio) propyl)pyridin-1-ium dibromide(SHE-2N), 3-(benzo[d]thiazol-2-yl)-6,8,8,9-tetramethyl-2-oxo-8,9-dihydro-2H-pyrano[3,2-g]quinoline-4-carbonitrile (SAG-38), Live Cell Imaging Solution (LCIS; Invitrogen), PBS-phosphate buffer saline (Gibco), 100× dcb: 100 times diluted bicarbonate buffer (pH 10, osmolarity 5 miliosmolar, mixed in-house), F-12K cell culture medium (Gibco), RPMI 1640 cell culture medium (Gibco), Trypsin (Sigma), penicillin–streptomycin (Sigma), non-essential amino acids (Gibco), Beta mercaptoethanol (Gibco), glucose (Kemika), bovine serum albumin (BSA) (Sigma), hydrogen peroxide (Merck), chlorpromazine (Alfa Aesar), methyl-beta-cyclodextran (MBCD; Acros organics), resveratrol (Sigma), #1.5H µ-dishes (Ibidi,) #1.5H µ-Slide 8-well (Ibidi), Limulus amebocyte lysate assay (Lonza, Walkersville, MD, USA), 10% neutral buffered formalin (CellPath, Ltd., UK), haematoxylin and eosin (H&E), Pelcotec SFG12 Finder Grid Substrate-Si wafers (Ted Pella), Aeroneb Pro nebulizer (from VITROCELL Cloud 6 system), GeneChip WT PLUS Reagent Kit (Thermo Fisher/Affymetrix), RNeasy Plus Mini Kit (Qiagen), WT PLUS Reagent Kit (Thermo Fisher Scientific, Inc., Waltham, USA), Mouse Clariom S arrays (Thermo Fisher Scientific).

Nanomaterials used in this study are as follows. TiO_2 nanotubes (PU-nTOX-01-03) and TiO_2 nanocubes (PU-nTOX-01-21) were synthesized in-house by P. Umek. Carbon black (Printex 90, kindly provided by Evonik, Frankfurt, Germany), TiO_2 MKNA015 (MKN-TiO_2-A015), TiO_2 MKNA100 (MKN-TiO_2-A100), and quartz silica (SiO_2 DQ12, kindly provided by, Craig Poland, IOM, Edinburgh, UK) were kind gift from U. Vogel. NM-101 TiO_2 anatase (TiO_2-NM101-JRCNM01001a), NM-105 TiO_2 rutil-anatase (TiO_2-NM105-JRCNM01005a), NM-110 ZnO (ZnO-NM110-JRCNM62101a), NM 111 ZnO (ZnO-NM111-JRCNM01101a), NM-200 SiO_2 (SiO_2-NM200-JRCNM02000a), NM-401 MWCNT (MWCNTs-NM401-JRCNM04001a), and NM-402 MWCNT (MWCNTs-NM402-JRCNM04002a) were a kind gift from JRC Nanomaterial Repository.

Softwares used in the study are as follows: Imspector (version 16.2.8282-metadata-win64-BASE) software provided by Abberior; SPCImage 7.3 (Becker & Hickl); Fiji, ImageJ 1.52p (NIH); syGlass (http://www.syglass.io/, RRID:SCR_017961); Mathematica 12.0, license L5063-5112 (Wolfram); genomics software: GSEA by Broad Institute; modeling: GROMACS 2018.3 (calculation), VMD (visualization).

TiO_2 Nanotubes Synthesis and Labeling: The TiO_2 anatase nanotubes used in this paper were synthesized, functionalized with AEAPMS, and labeled with STED-compatible fluorescent probes via a covalent reaction between the AEAPMS and ester functional group on the probe. All this was done in-house as described in reference.[40] Labeled TiO_2 was then stored suspended in 100× diluted bicarbonate buffer. For the multinanomaterial exposure experiments, other nanomaterials (NMs) were used as well. In this case, the nanomaterials were suspended in PBS and sonicated in ice bath using a tip sonicator (Sonicator 4000, Misonix, with 419 Microtip probe) for 15 min with 5s ON/5s OFF steps.

Cell Culture: Murine epithelial lung tissue cell line (LA-4; cat. no. ATCC CCL-196) and murine alveolar lung macrophage (MH-S; cat. No. CRL2019) cell line were purchased from and cultured according to American Type Culture Collection (ATCC) instructions. Cells were cultured in TPP cell culture flasks at 37 °C in a 5% CO_2 humidified atmosphere until monolayers reached desired confluency. All experiments were performed with cells before the twentieth passage. For long-term live cell experiments, a homemade stage-top incubator that maintains a humidified atmosphere with 5% CO_2 and is heated to 37 °C was used.

The medium used for culturing of the epithelial LA-4 cells was Ham's F-12K medium (Gibco) supplemented with 15% FCS (ATCC), 1% P/S

(Sigma), 1% NEAA (Gibco), 2×10^{-3} M L-gln. For alveolar macrophages cell line, MH-S, RPMI 1640 (Gibco) medium supplemented with 10% FCS (ATCC), 1% P/S (Sigma), 2×10^{-3} M L-gln, and 0.05×10^{-3} M beta mercapthoethanol (Gibco) was used.

In Vitro Sample Preparation and Exposure: LA-4 and MH-S cells were seeded in Ibidi 1.5H dishes of various surface area, depending on the experiment. After 24 h, nanomaterial ($c = 1$ mg mL^{-1}) was added at an appropriate surface dose (S_{NP}:S_{cells}), according to the experiment needs. Before exposure, nanomaterial suspension was sonicated for 10 s in an ultrasonic bath (Bransonic ultrasonic cleaner, Branson 2510EMT). Cells were then incubated at 37 °C and 5% CO_2 atmosphere with the nanomaterial for the desired time in order to observe the cells at the post-exposure time points of interest. If the experiment required monoculture of either cell line, sample were prepared as described above, if however, for experiments with the co-cultures, sample preparation differed slightly. For co-cultures, LA-4 and MH-S were grown in separate dishes up to desired confluency (lower than for monocultures) and then mixed them together by adding MH-S in the LA-4 dish at a ratio of 1: 40. Co-cultures were then incubated for 24 h more, exposed to nanomaterial as described above and incubated for additional desired amount of time. Growth medium for co-cultures was mixture of equal volumes of F-12K and RPMI 1640. Cells were then labeled with fluorescent dyes according to the manufacturer's recommendations. Right before observing the live cells, unbound fluorescent label was washed and medium was exchanged for LCIS.

In some experiments, different chemicals for modulation of the cell metabolism were used. For blocking the Clathrin-mediated endocytosis, cells were treated with 100×10^{-6} M chlorpromazine for 15 min. Membrane cholesterol was extracted with a 24 h incubation with 0.5–1 $\times$ 10^{-3} M MBCD. FAS was inhibited with overnight 100×10^{-6} M resveratrol incubation. Finally, for actin stabilization, higher concentration (≥1 $\times$ 10^{-3} M) of Sir-Actin Label based on Jasplankinolide was used. All the chemical modulators were added before exposure to nanomaterial and continued to be incubated with the cells even after during incubation with the nanomaterial for abovementioned time periods.

For the reuptake experiments, different cell lines were grown separately, and washed with PBS before adding MH-S to LA-4.

Samples for HIM and SEM were prepared as described above, except for cells being seeded on Si wafers instead of on glass-bottom dishes. After reaching desired confluency samples were freeze-dried with metal mirror freezing technique.

Fluorescence Imaging In Vitro: Super-resolution and confocal fluorescence micrographs were acquired using a customized STED microscope from Abberior with an Olympus IX83 microscope and two avalanche photodiodes as detectors (APDs). The microscope is equipped with two 120 picosecond pulsed laser sources (Abberior) with excitation wavelengths 561 and 640 nm and maximal power of 50 µW in the sample plane. Pulse repetition frequency for experiments was 40–80 MHz, depending on the experiment. STED depletion laser wavelength is 775 nm with same repetition frequency as excitation lasers, pulse length of 1.2 ns and maximal power of 170 mW in the sample plane. Filter sets used for detection were either 585–625 nm (green channel) or 650–720 nm (red channel). Images were acquired using Imspector (version 16.2.8282-win64) software also provided by Abberior. All microscope settings were tuned separately for maximal resolution during each of the experiments and are listed alongside the recorded images in the Supporting Information.

Fluorescence lifetime images (FLIM) were obtained on the same customized STED microscope (Abberior instruments) as confocal and STED fluorescence images in this study. This time, the emitted fluorescence was detected using PMT detectors and TCSPC technology developed by Becker & Hickl. 16-channel GaASP PMT detectors attached to a spectrograph with diffraction grating 600 l mm^{-1} were used to measure fluorescence lifetime of emitted photons with wavelengths ranging from 560 to 760 nm. Spectral information was discarded and the lifetimes were gathered in Imspector 16.2 (Abberior Instruments).

The fluorescence lifetime data was analyzed with SPCImage 7.3 software (Becker & Hickl), where the Decay matrix was calculated from the brightest pixel in the image (monoexponential fitting), binning was set to 3 and threshold to 5. The rainbow LUT was rescaled to range from 500 to 1000 ps for all images and both intensity and contrast of the lifetime-coded image were adjusted for easier comparison of lifetimes between samples.

Imaging of Nanomaterial in Backscatter Mode: In Figure 2C, simultaneously with measuring fluorescence from CellMask Orange in the cell membrane (as described above using STED), backscattered light was detected as well to locate the nanomaterial in the sample. A tunable Chameleon Discovery laser (Coherent) with 100 fs long pulses, pulse repetition frequency 80 MHz, and maximal average power of 1.7 W at 850 nm was used as the scattering light. The preattenuated laser light with a wavelength of 750 nm first passed through a 785 nm built-in dichroic where a fraction of the power was directed onto the sample through the same 60× WI objective (NA 1.2) as the excitation light for fluorescence imaging. The light scattered off the nanomaterial and passed back through the same objective and dichroic, now mostly passing through the dichroic toward the detectors. After passing through a pinhole (0.63 A.U.), the backscattered light was spectrally separated from the fluorescence by a short-pass 725 nm dichroic, afterward being detected on the same PMT as described above using FLIM, this time set to collect light with wavelengths above 725 nm.

Due to the large coherence of the laser, the backscattered light exhibited a strong speckle pattern, which was diminished by a 100-nm-wide Gaussian blur on the scattering image, thus decreasing false negative colocalization of nanomaterial on account of spatial resolution.

SEM Imaging:: The imaging was performed on MIRA3 Flexible FE-SEM produced by TESCAN, by detection of secondary electrons. Beam powers used have been between 5 and 15 kV with variable field of view 1.8–180 µm. All samples have been measured under high-pressure vacuum (HiVac). All analysis has been performed in Tescan developed software.

HIM Imaging: Super-resolution imaging on the nanoscale was carried out using a helium-ion microscope (HIM) (Orion NanoFab, Zeiss) available at IBC at the Helmholtz-Zentrum Dresden—Rossendorf e.V., a member of the Helmholtz Association. The microscope equipped with GFIS injection system and additional in-situ backscatter spectrometry and secondary ion mass spectrometry can achieve 0.5 nm lateral resolution imaging using 10–35 keV He ion beams. Measurements of secondary electrons (Se) emitted from the first few nanometers of the sample were done by He ion acceleration of 30 keV, current of 1.7 pA and were acquired under high vacuum inside the sample chamber (3×10^{-7} mBar). Field-of-view was varied from 60 µm × 60 µm down to 1 µm × 1 µm, with pixel steps small as 2 nm. Imaging was performed on non-tilted and tilted sample stage (45°) for better 3D visualization.

TEM Imaging: For ZnO and coated ZnO, the imaging was done as follows: 1 mg of each material was dispersed in 1 mL MilliQ water, apart from CNTs, which were dispersed in 1 mL tannic acid solution 300 mg L^{-1} using a vial tweeter for 15 min. Each suspension was diluted 1/10 and 3 µL drop deposited on Formvar Carbon coated 200 mesh copper grids (Agar Scientific, USA) and dehydrated overnight in a desiccator before analysis. Images were collected using a JEOL JEM-2100 HR-transmission electron microscope at 120 kV (JEOL, Italy) at JRC.[54]

For TEM imaging of TiO_2 nanotubes, the nanoparticles were dispersed in water and the dispersion sonicated in water bath for ≈3 h before use. Of each sample 5 µL was deposed onto glow-discharged copper grid (Agar scientific, Ltd., UK) for 1 min and the excess of sample was removed blotting with filter paper. After shortly washing with one drop of water, the grid was therefore immersed into a 2% uranyl acetate (UA) solution for 20 s and blotted again with filter paper. The grids were imaged using a JEOL JEM-2100F fitted with a Gatan Orius SC 1000 camera (2 × 4k).

Transcriptomics In Vitro: Cells were grown in 6-well plates and exposed to TiO_2 nanotubes for 4 h and 48 h, control samples were taken at 0 h and 48 h. Samples were prepared as described above. Briefly, growth medium was removed and the 6-well plates containing cells only were frozen at –70 °C. Total RNA was isolated employing the RNeasy Plus Mini Kit (Qiagen). The Agilent 2100 Bioanalyzer was used to assess RNA quality and RNA with RIN > 7 was used for microarray analysis.

Total RNA (120 ng) was amplified using the WT PLUS Reagent Kit (Thermo Fisher Scientific, Inc., Waltham, USA). Amplified cDNA was hybridized on Mouse Clariom S arrays (Thermo Fisher Scientific). Staining and scanning (GeneChip Scanner 3000 7G) was done according to manufacturer's instructions.

Statistical analysis for all probe sets included limma *t*-test and Benjamini–Hochberg multiple testing correction. Raw *p*-values of the limma *t*-test were used to define sets of regulated genes ($p < 0.01$). Detection above background (dabg) *p*-values were used to exclude background signals: significant genes were filtered for $p < 0.05$ in more than half of the samples in at least one group. Array data has been submitted to the GEO database at NCBI (GSE146036).

In the arrow graphs, only genes which were up- or downregulated more than two times compared to non-exposed cells are shown. The signal (*x*-axis) is drawn in logarithmic scale. Expression is normalized to expression of control samples.

In Vivo Data: TiO_2 nanotubes were suspended in nanopure water with 2% v/v mouse serum (prepared in-house) to a final concentration of 3.24 mg mL^{-1}. The suspension was probe sonicated on ice for 16 min with 10% amplitude. 3.24 mg mL^{-1} corresponds to a dose of 162 µg TiO_2 nanotubes per 50 µL instillation volume per mice. The vehicle of nanopure water with 2% v/v mouse serum was probe sonicated using the same protocol. The dose of 162 µg per mouse corresponds to an average surface dose of 1:2 ($S_{nanomaterials}$:S_{cells}) and is equivalent to 15 working days at the 8-h time-weighted average occupational exposure limit for TiO_2 by Danish Regulations (6.0 mg m^{-3} TiO_2).

The average hydrodynamic particle size of the TiO_2 nanotube in suspension (3.24 mg mL^{-1}) was determined by dynamic light scattering (DLS). The TiO_2 nanotube suspension had a bimodal size distribution with a major peak at 60 nm and a narrow peak at 21 nm.[10] The intensity-based average size was 168.7 nm and the polydispersity index (PI) was 0.586, indicating some polydispersity in the suspensions. Endotoxin levels were measured using the Limulus Amebocyte Lysate Assay. The level of endotoxins was low in TiO_2 tube suspensions (0.095 endotoxin units [EU]), and in nanopure water with 2% mouse serum (0.112 EU mL^{-1}).

Seven-week-old female C57BL/6jBomtac mice (Taconic, Ejby, Denmark) were randomized in groups for TiO_2 nanotube exposure ($N = 5$ mice per group for histology) and vehicle controls ($N = 2$–4 mice per group). At 8 weeks of age, the mice were anaesthetized and exposed to 0 µg or 162 µg TiO_2 nanotube in 50 µL vehicle by single intratracheal instillation. In brief, the mice were intubated in the trachea using a catheter. The 50 µl suspension was instilled followed by 200 µL air. The mouse was transferred to a vertical hanging position with the head up. This ensures that the administered material is maintained in the lung. Animal experiments were performed according to EC Directive 2010/63/UE in compliance with the handling guidelines established by the Danish government and permits from the Experimental Animal Inspectorate (nos. 2015-15-0201-00465 and 2010/561-1179). Prior to the study, the experimental protocols were approved by the local Animal Ethics Council. More details regarding the animal study can be found in ref. [10].

Histology and Enhanced Dark-Field Imaging: At 28, 90, or 180 days post-exposure mice were weighed and anesthetized. Lungs were filled slowly with 4% formalin under 30 cm water column pressure. A knot was made on the trachea to secure formaldehyde in lungs to fixate tissue in "inflated state." Lungs were then removed and placed in 4% neutral buffered formaldehyde for 24 h. After fixation, the samples were trimmed, dehydrated and embedded in paraffin. 3 µm thin sections were cut and stained with haematoxylin and eosin (H&E). Cytoviva enhanced dark-field hyperspectral system (Auburn, AL, USA) was used to image particles and organic debris in the histological sections of mouse lungs. Enhanced dark-field images were acquired at 100× on an Olympus BX 43 microscope with a Qimaging Retiga4000R camera.

Transcriptomics In Vivo: Microarray mRNA analysis was performed using Agilent 8x60K oligonucleotide microarrays (Agilent Technologies, Inc., Mississauga, ON, Canada) as described previously[55] with six replicas for each condition. Bioinformatics analysis of the row data: signal intensities were Loess normalized using the limma package in R/Bioconductor.[56] Analysis of differentially expressed genes (DEGs) was performed using the limma package. The genes were considered as significantly differentially expressed if the BH-adjusted *p*-values were less than or equal to 0.1. Statistical analysis is same as for the in vitro transcriptomics above.

Comparison of Transcriptomics In Vitro and In Vivo: Mice were exposed to 18, 54, or 162 µg of TiO_2 nanotubes per mouse and lungs were harvested on 1st and 28th day post exposure for transcriptomic analysis to evaluate overlapping sets of genes differentially expressed in the in vivo and in vitro experimental data. The goal of the analysis is to determine and compare alterations in lipid metabolism, immune response in terms of proinflammatory signaling and cholesterol metabolism between two experimental systems. For the assessment of the monocyte influx, all genes encoding monocyte chemoattractive (C–C motif) chemokines were selected and their expression evaluated.

Atomistic Molecular Dynamics Simulation: The simulations have beed carried out for DMPC and POPE lipids near anatase (101) TiO_2 surface in water environment. Anatase slab (71.8 × 68.2 × 30.5 Å) with (101) surface normal to the *z*-axis is used as a model of a nanoparticle surface. The slab contains 4536 Ti atoms of which 504 are fivefold coordinated atoms on the surface. (101) anatase surface was chosen as a surface of the lowest energy. At neutral pH TiO_2 surface is covered by hydroxyl groups and is negatively charged. In this model, hydroxyl groups were made to bind to 5-coordinated surface Ti atoms so that the surface charge density is close to the experimental value at neutral pH. Thus, 151 hydroxyl groups were added to randomly picked Ti surface atoms (which constitutes 30% of their total amount) which results in a surface charge density of –0.62 electrons nm^{-2}, which is in line with the experimental results.[57]

The TiO_2 slab is then placed in the middle of the simulation box with 3D periodic boundary conditions. The box size in *X*- and *Y*-directions is defined by the slab length and width so that the slab is periodic in those directions. The height of the box is set to 130 Å to accommodate the TiO_2 slab (thickness of 30.5 Å), eventual formed lipid bilayer on the both sides (2 × 40 Å) as well as their hydration layers (2 × 10 Å). 82 lipid molecules (POPE or DMPC) are inserted at random unoccupied positions in the box in random orientations, after that the box is filled with water molecules (about 12 000). Then, a small number of water molecules are picked at random and are substituted with Na^+ and Cl^- ions to balance the negative surface charge of the slab and provide NaCl concentration of 0.15 M in the water phase of the simulated system.

First, energy minimization of the simulated systems using the steepest gradient descent method is performed, followed by a short 100 ps pre-equilibration run at constant volume and temperature. After that, the pressure in the system is equilibrated to 1 bar using anisotropic Berendsen barostat[58] with relaxation time of 5 ps during 10 ns, which is finally followed by 1 µs production run in the NVT ensemble. Leap-frog algorithm with time step 1 fs is used to integrate the equations of motion. Center-of-mass motion is removed every 100 steps. Verlet cut-off scheme[59] with the buffer tolerance of 0.005 kJ mol^{-1} ps^{-1} per atom is used to generate the pair lists. Minimum cut-off of 1.4 nm is used for both short-ranged electrostatic and VdW interactions. Long-range electrostatics are calculated using PME[60] with the grid spacing of 0.12 nm and cubic interpolation. Long-range dispersion corrections are applied to both energy and pressure. Velocity rescaling thermostat[61] is used to control the temperature, which is set to 303 K with the relaxation time of 1 ps. All bonds with hydrogen atoms are constrained using the LINCS algorithm.[62] Atom coordinates and energies are saved every 5 ps. All simulations were performed by the Gromacs 2019 software package.[63] Visualization of the simulations is done by VMD.[64]

Lipids are described by the Slipids force field.[65] For TiO_2, parameters optimized to fit results on charge density distributions were used and water–TiO_2 surface coordination obtained in ab initio simulations of TiO_2-water interface.[66] These parameters are listed in tables in Section S3e, Supporting Information. Water molecules are represented by the TIP3P model,[67] and for Na^+ and Cl^- ions Yoo and Aksimentiev ion parameters are used.[68] Lorentz–Berthelot rules are applied to determine Lennard-Jones parameters for cross-interactions.

Model of Chronic Inflammation: The theoretical model of chronic inflammation following nanomaterial exposure is described by a series of differential equations (Section S6a, Supporting Information), describing the events observed in in vitro and in vivo experiments in this work. This minimal-complexity in vivo model consists of six variables (surface of nanomaterial in epithelial cells, in cauliflowers, in macrophages and freely floating nanomaterial, surface of macrophages and surface of epithelial cells), four fixed parameters which are calibrated for each model system and later locked (endocytosis rate, rate of cauliflower endocytosis, delay between cauliflower formation and signaling for macrophage influx, and epithelial cell replication rate) and 3 NM-associated parameters (cauliflower formation rate *cff*, signaling efficiency *signEff*, and toxicity *tox*). Separate in vitro models were obtained from the in vivo model by swapping the macrophage influx with macrophage replication and leaving out non-existent cells for monocultures.

The system of equations was solved numerically using Wolfram Mathematica 12.0, license L5063-5112, to obtain the time evolution and final state of the model. The same software was also used for visualization of the results.

The phase space was scanned by calculating the time evolution of the appropriate system of equations from chapter S6a for a set of nanomaterials with appropriately interspaced parameters: toxicity (*tox*), cauliflower formation (*cff*), and signaling efficiency (*signalEff*). For each parameter, 30 logarithmically equally spaced values in a sensible range were chosen—the total amount of values in the grid was thus $30 \times 30 \times 30 = 27.000$.

Supporting Information

Supporting Information is available from the Wiley Online Library or from the author.

Acknowledgements

The authors are grateful to the team at TeScan for FE-SEM measurements and would like to thank G. Hlawacek and N. Klingner (HZDR) for assistance on HIM. They thank K. Richter for excellent technical assistance for the transcriptomics analysis, J. Birkelund Sørli with in vivo experiments, as well as A. Williams, L. Rahman, and A. Limersan (Health Canada) for their help. They kindly thank JRC Nanomaterials Repository for providing them with various nanomaterials and the team from Syglass for their support. They thank the anonymous reviewers whose support, suggestions, and in-depth comments majorly improved this manuscript. This research was funded by the EU Horizon 2020 Grant No. 686098 (SmartNanoTox project), Slovenian Research Agency (program P1-0060), Slovenian Research Agency Young Researcher Program (H.K.), Slovenian Research Agency Young Researcher Program (A.S.), the Helmholtz Alliance "Aging and Metabolic Programming, AMPro" (J.B.), Genomics Research and Development Initiative and Chemicals Management Plan of Health Canada (S.H.), China Scholarship Council (CSC fellowship 201806240314 to Q.Z.), and Science Foundation Ireland (grant 16/IA/4506 to V.L.). Crossing borders and scales - an interdisciplinary approach (CROSSING project, PIE-0007) (R.P.).

Note: The first name and surnames of author Carolina Ballester-López were misidentified in the originally published version. This was corrected on November 24, 2020, after initial publication online.

Conflict of Interest

The authors declare no conflict of interest.

Author Contributions

H.K., B.K., and A.S. contributed equally to this work. The manuscript was written through contributions of all authors. All authors have given approval to the final version of the manuscript. H.K., B.K., A.S., C.V., R.P., P.Z., T.B., C.B.L., P.H.D., C.C., V.Z., M.S., O.J., M.Ir., J.B., V.L., S.H., N.Q., A.L., U.V., T.K., T.S., and J.S. designed the study and analysis. H.K., B.K., A.S., C.V., R.P., P.Z., T.B., P.H.D., C.C., A.K., P.C., Q.Z., J.P., Z.D., M.P., P.U., S.P., M.Ir., and S.H. prepared the samples. H.K., B.K., A.S., C.V., R.P., P.Z., T.B., P.H.D., C.C., A.K., P.C., Q.Z., J.P., Z.D., M.P., M.Ir., and S.H. performed the experiments. H.K., B.K., A.S., C.V., R.P., P.Z., T.B., C.B.L., C.C., A.K., Q.Z., J.P., V.Z., Z.D., M.P., M.Ir., J.B., S.H., T.K., T.S., and J.S. analyzed the data. H.K., M.Iv., and M.S. performed the modeling. O.J., J.B., V.L., S.H., N.Q., A.L., U.V., T.K., T.S., and J.S. supervised the study. H.K., B.K., and A.S. prepared the manuscript with input from all other authors.

Keywords

advanced microscopies, adverse outcome pathways, disease prediction, material safety and health hazards, mode of action

Received: June 8, 2020
Revised: August 22, 2020
Published online: October 19, 2020

[1] S. J. Klaine, P. J. J. Alvarez, G. E. Batley, T. F. Fernandes, R. D. Handy, D. Y. Lyon, S. Mahendra, M. J. McLaughlin, *J. R. Lead, Environ. Toxicol. Chem.* **2008**, *27*, 1825.
[2] P. Biswas, C.-Y. Wu, *J. Air Waste Manag. Assoc.* **2005**, *55*, 708.
[3] R. D. Handy, R. Owen, E. Valsami-Jones, *Ecotoxicology* **2008**, *17*, 315.
[4] OECD, *OECD Environmental Outlook, Organization for Economic Cooperation and Development*, Paris, France **2012**.
[5] WHO, *Air Pollution*, https://www.who.int/westernpacific/health-topics/air-pollution (accessed: August 2020).
[6] J. Lelieveld, K. Klingmüller, A. Pozzer, U. Pöschl, M. Fnais, A. Daiber, T. Münzel, *Eur. Heart J.* **2019**, *40*, 1590.
[7] C. R. Navarrette, J. H. Sisson, E. Nance, D. Allen-Gipson, J. Hanes, T. A. Wyatt, *J. Aerosol Med. Pulm. Drug Delivery* **2012**, *25*, 159.
[8] W. G. Kreyling, M. Semmler-Behnke, W. Möller, *J. Aerosol Med.* **2006**, *19*, 74.
[9] W. G. Kreyling, M. Semmler-Behnke, S. Takenaka, W. Möller, *Acc. Chem. Res.* **2013**, *46*, 714.
[10] P. H. Danielsen, K. B. Knudsen, J. Štrancar, P. Umek, T. Koklič, M. Garvas, E. Vanhala, S. Savukoski, Y. Ding, A. M. Madsen, N. R. Jacobsen, I. K. Weydahl, T. Berthing, S. S. Poulsen, O. Schmid, H. Wolff, U. Vogel, *Toxicol. Appl. Pharmacol.* **2020**, *386*, 114830.
[11] K. Fujita, M. Fukuda, H. Fukui, M. Horie, S. Endoh, K. Uchida, M. Shichiri, Y. Morimoto, A. Ogami, H. Iwahashi, *Nanotoxicology* **2015**, *9*, 290.
[12] W.-S. Cho, R. Duffin, M. Bradley, I. L. Megson, W. Macnee, S. E. M. Howie, K. Donaldson, *Eur. Respir. J.* **2012**, *39*, 546.
[13] S. van den Brule, E. Beckers, P. Chaurand, W. Liu, S. Ibouraadaten, M. Palmai-Pallag, F. Uwambayinema, Y. Yakoub, A. Avellan, C. Levard, V. Haufroid, E. Marbaix, A. Thill, D. Lison, J. Rose, *Part. Fibre Toxicol.* **2014**, *11*, 67.
[14] F. Tian, N. C. Habel, R. Yin, S. Hirn, A. Banerjee, N. Ercal, S. Takenaka, G. Estrada, K. Kostarelos, W. Kreyling, T. Stoeger, *Eur. J. Pharm. Biopharm.* **2013**, *84*, 412.
[15] S.-H. Kim, S. Jeon, D.-K. Lee, S. Lee, J. Jeong, J. S. Kim, W.-S. Cho, *Nanotoxicology* **2020**, *14*, 468.

[16] E. Underwood, *Science* **2017**, *355*, 342.
[17] V. Stone, M. R. Miller, M. J. D. Clift, E. Alison, N. L. Mills, P. Møller, R. P. F. Schins, U. Vogel, W. G. Kreyling, A. J. Keld, T. A. J. Kuhlbusch, P. E. Schwarze, P. Hoet, A. Pietroiusti, A. D. Vizcaya-Ruiz, A. Baeza-Squiban, J. P. Teixeira, C. L. Tran, F. R. Cassee, *Environ. Health Perspect.* **2017**, *125*, 106002.
[18] M. A. Bañares, A. Haase, L. Tran, V. Lobaskin, G. Oberdörster, R. Rallo, J. Leszczynski, P. Hoet, R. Korenstein, B. Hardy, T. Puzyn, *Nanotoxicology* **2017**, *11*, 839.
[19] A. J. Clippinger, A. Ahluwalia, D. Allen, J. C. Bonner, W. Casey, V. Castranova, R. M. David, S. Halappanavar, J. A. Hotchkiss, A. M. Jarabek, M. Maier, W. Polk, B. Rothen-Rutishauser, C. M. Sayes, P. Sayre, M. Sharma, V. Stone, *Arch. Toxicol.* **2016**, *90*, 1769.
[20] J. R. Rohr, C. J. Salice, R. M. Nisbet, *Science* **2017**, *356*, 917.
[21] D. Huh, B. D. Matthews, A. Mammoto, M. Montoya-Zavala, H. Y. Hsin, D. E. Ingber, *Science* **2010**, *328*, 1662.
[22] V. Forest, J.-F. Hochepied, J. Pourchez, *Chem. Res. Toxicol.* **2019**, *32*, 1320.
[23] S. Dekkers, A. G. Oomen, E. A. J. Bleeker, R. J. Vandebriel, C. Micheletti, J. Cabellos, G. Janer, N. Fuentes, S. Vázquez-Campos, T. Borges, M. J. Silva, A. Prina-Mello, D. Movia, F. Nesslany, A. R. Ribeiro, P. E. Leite, M. Groenewold, F. R. Cassee, A. J. A. M. Sips, A. Dijkzeul, T. van Teunenbroek, S. W. P. Wijnhoven, *Regul. Toxicol. Pharmacol.* **2016**, *80*, 46.
[24] A. D. Maynard, R. J. Aitken, *Nat. Nanotechnol.* **2016**, *11*, 998.
[25] A. E. Nel, T. F. Malloy, *Science* **2017**, *355*, 1016.
[26] B. Drasler, P. Sayre, K. G. Steinhäuser, A. Petri-Fink, B. Rothen-Rutishauser, *NanoImpact* **2017**, *8*, 99.
[27] U.S. Environmental Protection Agency, "Provisional Assessment of Recent Studies on Health Effects of Particulate Matter Exposure", https://www3.epa.gov/ttn/naaqs/standards/pm/data/20121213psa.pdf (accessed: June 2020).
[28] J. D. Ede, V. Lobaskin, U. Vogel, I. Lynch, S. Halappanavar, S. H. Doak, M. G. Roberts, J. A. Shatkin, *Nanomaterials* **2020**, *10*, 1229.
[29] S. Halappanavar, S. van den Brule, P. Nymark, L. Gaté, C. Seidel, S. Valentino, V. Zhernovkov, P. H. Danielsen, A. De Vizcaya, H. Wolff, T. Stöger, A. Boyadziev, S. S. Poulsen, J. B. Sørli, U. Vogel, *Part. Fibre Toxicol.* **2020**, *17*, 16.
[30] K. Rasmussen, J. Mast, P.-J. De Temmerman, E. Verleysen, N. Waegeneers, F. Van Steen, J. C. Pizzolon, L. De Temmerman, E. Van Doren, K. A. Jensen, R. Birkedal, M. Levin, S. H. Nielsen, I. K. Koponen, P. A. Clausen, V. Kofoed-Sørensen, Y. Kembouche, N. Thieriet, O. Spalla, C. Giuot, D. Rousset, O. Witschger, S. Bau, B. Bianchi, C. Motzkus, B. Shivachev, L. Dimowa, R. Nikolova, D. Nihtianova, M. Tarassov, O. Petrov, S. Bakardjieva, D. Gilliland, F. Pianella, G. Ceccone, V. Spampinato, G. Cotogno, P. Gibson, C. Gaillard, A. Mech, *Titanium Dioxide, NM-100, NM-101, NM-102, NM-103, NM-104, NM-105: Characterisation and Physico-Chemical Properties*, Publications Office Of The European Union, Luxembourg **2014**.
[31] L. Rahman, D. Wu, M. Johnston, A. William, S. Halappanavar, *Mutagenesis* **2017**, *32*, 59.
[32] K. Rasmussen, A. Mech, J. Mast, P.-J. De Temmerman, N. Waegeneers, F. Van Steen, J. C. Pizzolon, L. De Temmerman, E. Van Doren, K. A. Jensen, R. Birkedal, M. Levin, S. H. Nielsen, I. K. Koponen, P. A. Clausen, Y. Kembouche, N. Thieriet, O. Spalla, C. Giuot, D. Rousset, O. Witschger, S. Bau, B. Bianchi, B. Shivachev, D. Gilliland, F. Pianella, G. Ceccone, G. Cotogno, H. Rauscher, P. Gibson, H. Stamm, *Synthetic Amorphous Silicon Dioxide (NM-200, NM-201, NM-202, NM-203, NM-204): Characterisation and Physico-Chemical Properties*, Publications Office Of The European Union, Luxembourg **2013**.
[33] C. Singh, S. Friedrichs, M. Levin, R. Birkedal, K. A. Jensen, G. Pojana, W. Wohlleben, S. Schulte, K. Wiench, T. Turney, D. Koulaeva, D. Marshall, K. Hund-Rinke, W. Koerdel, E. Van Doren, P.-J. De Temmerman, M. A. D. Francisco, J. Mast, P. Gibson, R. Koeber, T. Linsinger, C. Klein, *NM-Series of Representative Manufactured Nanomaterials – Zinc Oxide NM-110, NM-111, NM-112, NM-113: Characterisation and Test Item Preparation*, Publications Office Of The European Union, Luxembourg **2011**.
[34] N. Hadrup, F. Rahmani, N. R. Jacobsen, A. T. Saber, P. Jackson, S. Bengtson, A. Williams, H. Wallin, S. Halappanavar, U. Vogel, *Nanotoxicology* **2019**, *13*, 1275.
[35] K. Rasmussen, J. Mast, P.-J. De Temmerman, E. Verleysen, N. Waegeneers, F. Van Steen, J. C. Pizzolon, L. De Temmerman, E. Van Doren, K. A. Jensen, R. Birkedal, P. A. Clausen, Y. Kembouche, N. Thieriet, O. Spalla, C. Giuot, D. Rousset, O. Witschger, S. Bau, B. Bianchi, B. Shivachev, L. Dimowa, R. Nikolova, D. Nihtianova, M. Tarassov, O. Petrov, S. Bakardjieva, C. Motzkus, G. Labarraque, C. Oster, G. Cotogno, C. Gaillard, *Multi-Walled Carbon Nanotubes, NM-400, NM-401, NM-402, NM-403: Characterisation and Physico-Chemical Properties*, Publications Office Of The European Union, Luxembourg **2014**.
[36] Unpublished results from NRCWE, obtained in SmartNanoTox project, **2020**.
[37] S. S. Poulsen, A. T. Saber, A. Williams, O. Andersen, C. Købler, R. Atluri, M. E. Pozzebon, S. P. Mucelli, M. Simion, D. Rickerby, A. Mortensen, P. Jackson, Z. O. Kyjovska, K. Mølhave, N. R. Jacobsen, K. A. Jensen, C. L. Yauk, H. Wallin, S. Halappanavar, U. Vogel, *Toxicol. Appl. Pharmacol.* **2015**, *284*, 16.
[38] J. A. Bourdon, A. T. Saber, N. R. Jacobsen, K. A. Jensen, A. M. Madsen, J. S. Lamson, H. Wallin, P. Møller, S. Loft, C. L. Yauk, U. B. Vogel, *Part. Fibre Toxicol.* **2012**, *9*, 5.
[39] T. L. Moore, D. A. Urban, L. Rodriguez-Lorenzo, A. Milosevic, F. Crippa, M. Spuch-Calvar, S. Balog, B. Rothen-Rutishauser, M. Lattuada, A. Petri-Fink, *Sci. Rep.* **2019**, *9*, 900.
[40] I. Urbančič, M. Garvas, B. Kokot, H. Majaron, P. Umek, H. Cassidy, M. Škarabot, F. Schneider, S. Galiani, Z. Arsov, T. Koklic, D. Matallanas, M. Čeh, I. Muševič, C. Eggeling, J. Štrancar, *Nano Lett.* **2018**, *18*, 5294.
[41] L. Yang, A. Feuchtinger, W. Möller, Y. Ding, D. Kutschke, G. Möller, J. C. Schittny, G. Burgstaller, W. Hofmann, T. Stoeger, D. Razansky, A. Walch, O. Schmid, *ACS Nano* **2019**, *13*, 1029.
[42] S. Dasgupta, T. Auth, G. Gompper, *Nano Lett.* **2014**, *14*, 687.
[43] T. D. Pollard, J. A. Cooper, *Science* **2009**, *326*, 1208.
[44] D. T. Tran, A. Masedunskas, R. Weigert, K. G. T. Hagen, *Nat. Commun.* **2015**, *6*, 1.
[45] S. Y. Khaitlina, *Biochem. Biokhimiia* **2014**, *79*, 917.
[46] P. Li, A. T. Bademosi, J. Luo, F. A. Meunier, *Trends Cell Biol.* **2018**, *28*, 685.
[47] D. T. Tran, K. G. T. Hagen, *J. Cell. Sci.* **2017**, *130*, 1355.
[48] D. L. Laskin, R. Malaviya, J. D. Laskin, in *Comparative Biology of the Normal Lung*, 2nd ed. (Ed.: R. A. Parent), Academic Press, San Diego, CA, USA **2015**, pp. 629–649.
[49] G. Oberdörster, E. Oberdörster, J. Oberdörster, *Environ. Health Perspect.* **2005**, *113*, 823.
[50] A. T. Saber, N. R. Jacobsen, P. Jackson, S. S. Poulsen, Z. O. Kyjovska, S. Halappanavar, C. L. Yauk, H. Wallin, U. Vogel, *WIRES Nanomed. Nanobiotechnol.* **2014**, *6*, 517.
[51] I. Gosens, A. Kermanizadeh, N. R. Jacobsen, A.-G. Lenz, B. Bokkers, W. H. de Jong, P. Krystek, L. Tran, V. Stone, H. Wallin, T. Stoeger, F. R. Cassee, *PLoS ONE* **2015**, *10*, e0126934.
[52] L. Di Cristo, M. G. Bianchi, M. Chiu, G. Taurino, F. Donato, G. Garzaro, O. Bussolati, E. Bergamaschi, *Nanomaterials* **2019**, *9*, 982.
[53] K. Bhattacharya, G. Kiliç, P. M. Costa, B. Fadeel, *Nanotoxicology* **2017**, *11*, 809.
[54] JRC, JRC Nanomaterials repository, https://ec.europa.eu/jrc/en/scientific-tool/jrc-nanomaterials-repository (accessed: March 2020).

[55] S. S. Poulsen, N. R. Jacobsen, S. Labib, D. Wu, M. Husain, A. Williams, J. P. Bøgelund, O. Andersen, C. Købler, K. Mølhave, Z. O. Kyjovska, A. T. Saber, H. Wallin, C. L. Yauk, U. Vogel, S. Halappanavar, *PLoS ONE* **2013**, *8*, e80452.
[56] M. E. Ritchie, B. Phipson, D. Wu, Y. Hu, C. W. Law, W. Shi, G. K. Smyth, *Nucleic Acids Res.* **2015**, *43*, e47.
[57] K. C. Akratopulu, L. Vordonis, A. Lycourghiotis, *J. Chem. Soc., Faraday Trans. 1* **1986**, *82*, 3697.
[58] H. J. C. Berendsen, J. P. M. Postma, W. F. van Gunsteren, A. DiNola, J. R. Haak, *J. Chem. Phys.* **1984**, *81*, 3684.
[59] S. Páll, B. Hess, *Comput. Phys. Commun.* **2013**, *184*, 2641.
[60] T. Darden, D. York, L. Pedersen, *J. Chem. Phys.* **1993**, *98*, 10089.
[61] G. Bussi, D. Donadio, M. Parrinello, *J. Chem. Phys.* **2007**, *126*, 014101.
[62] B. Hess, *J. Chem. Theory Comput.* **2008**, *4*, 116.
[63] M. J. Abraham, T. Murtola, R. Schulz, S. Páll, J. C. Smith, B. Hess, E. Lindahl, *SoftwareX* **2015**, *1–2*, 19.
[64] W. Humphrey, A. Dalke, K. Schulten, *J. Mol. Graph* **1996**, *14*, 33.
[65] J. P. M. Jämbeck, A. P. Lyubartsev, *J. Phys. Chem. B* **2012**, *116*, 3164.
[66] L. Agosta, E. G. Brandt, A. P. Lyubartsev, *J. Chem. Phys.* **2017**, *147*, 024704.
[67] W. L. Jorgensen, J. Chandrasekhar, J. D. Madura, R. W. Impey, M. L. Klein, *J. Chem. Phys.* **1983**, *79*, 926.
[68] J. Yoo, A. Aksimentiev, *J. Phys. Chem. Lett.* **2012**, *3*, 45.